



ELSEVIER

Contents lists available at ScienceDirect

Journal of Membrane Science

journal homepage: www.elsevier.com/locate/memsci

Highly water-selective hybrid membrane by incorporating g-C₃N₄ nanosheets into polymer matrix

Keteng Cao^{a,b}, Zhongyi Jiang^{a,b}, Xiaoshan Zhang^{a,b}, Yamin Zhang^{a,b}, Jing Zhao^{a,b},
Ruisi Xing^{a,b}, Sen Yang^{a,b}, Chengyun Gao^{a,b}, Fusheng Pan^{a,b,*}

^a Collaborative Innovation Center of Chemical Science and Engineering (Tianjin), Tianjin 300072, China

^b Key Laboratory for Green Chemical Technology of Ministry of Education, School of Chemical Engineering and Technology, Tianjin University, Tianjin 300072, China

ARTICLE INFO

Article history:

Received 21 November 2014

Received in revised form

29 March 2015

Accepted 26 April 2015

Available online 5 May 2015

Keywords:

Water-selective membrane

Hybrid membrane

g-C₃N₄ nanosheet

Sieving effect

Pervaporation

ABSTRACT

In this study, highly water-selective hybrid membranes with superior water/ethanol separation performance were fabricated by incorporating g-C₃N₄ nanosheets (CNs) into sodium alginate (SA) matrix. CNs were synthesized by thermal oxidation “etching” and ultrasound exfoliation methods, and their ultrathin and nanoporous structures were characterized by atomic force microscopy, Fourier transform infrared spectra, X-ray photoelectron spectroscopy, and X-ray diffraction. Due to the strong interfacial interactions between CNs and SA chains, the hybrid membranes exhibited higher mechanical strength and swelling resistance. Particularly, the horizontally aligned lamellar structure of CNs within hybrid membranes could render ordered channels for water transport, whereas the nanoporous structure of CNs could render additional sieving effect. Moreover, the intervention of CNs on polymer chain packing could render decreased crystallinity. Accordingly, the hybrid membranes exhibited excellent water permeability and selectivity for water/ethanol mixture separation. Especially, for the membrane containing 3 wt% CNs, the permeation flux could reach 2469 g/m² h while the separation factor was as high as 1653 under 76 °C and 10 wt% feed water concentration. Meanwhile, the hybrid membranes showed good long-term stability. This study could be extended to fabricate a variety of CNs-incorporated membranes for diverse liquid mixture or gas mixture separations.

© 2015 Elsevier B.V. All rights reserved.

1. Introduction

Nowadays, driven by the resource and energy demands for separating water from ions and molecules [1], water-selective membranes have received extensive attentions owing to their affordable, efficient and sustainable advantages [2]. Particularly, dense water-selective membranes are utilized for organic solution dehydration during the production of renewable biofuels [3]. Due to little differences in size and other physical properties of the molecules, preparing membranes with both high permeability and high selectivity remains a big challenge, especially the polymeric dense membranes [4,5]. Arisen from the intrinsic gambling between polymer chain stiffness and interchain spacing [6], polymeric water-selective membranes inevitably suffer from tradeoff effect [4,7], which means more permeable membranes are simultaneously less selective, and vice versa. Hence, fabricating

high performance water-selective membranes becomes crucial for efficient process intensification.

Most recently, ultrafast water permeation through graphene-derived membranes has been discovered [8], rendering these two-dimensional (2D) carbon materials promising candidates for developing water-selective membranes [9–13]. Within the interconnected 2D channels of graphene-stacked membranes, the nearly frictionless graphitic surface facilitates the fast flow of water molecules while the narrow channel can block other larger-sized species [8,9,11]. Prompted by these unique transport properties, Aminabhavi et al. [14,15] developed hybrid membranes embedded with functionalized graphene sheets, which exhibited enhanced performance for ethanol and isopropanol dehydration. In our previous study, it was found that more structural defects on GO nanosheets were favor of increasing water channels [16]. However, the amount of structural defects is rather limited even for reduced GO nanosheets [17]. Since GO nanosheets align themselves parallel to the membrane surface, water still follows a relatively tortuous path across the membrane causing a high transport resistance. Thus, graphene nanosheets with more porous structure (such as defects and wrinkles) are desirable to shorten the transport path and ensure a higher water flux [9,18,19].

* Corresponding author at: Key Laboratory for Green Chemical Technology of Ministry of Education, School of Chemical Engineering and Technology, Tianjin University, Tianjin 300072, China. Tel./fax: +86 22 23500086.

E-mail address: fspan@tju.edu.cn (F. Pan).

Besides, graphene membranes with well-defined size-selective nanopores were predicted to have great potential for high water permeation and efficient separation [20]. Because the large-scale manufacturing of graphene nanosheets with high porosity and controllable pore size remains challenging [10,18], newly nanoporous 2D materials need to be exploited for further enhancing the separation performance.

Graphitic carbon nitride ($g\text{-C}_3\text{N}_4$), an emerging graphene-analogue material, has attracted great attention due to its outstanding thermal and chemical stability, unique optical and photoelectrochemical property, as well as facile and inexpensive synthesis [21]. The bulk $g\text{-C}_3\text{N}_4$ can be easily exfoliated into 2D $g\text{-C}_3\text{N}_4$ nanosheets (CNs). In contrast to graphene and GO nanosheets, tri-*s*-triazine-based CNs, the most energetically stable form of CNs, possesses regularly distributed triangular nanopores throughout the entire laminar structure (Scheme 1(a)) [22]. Geometric diameter of the triangular nanopores is calculated to be approximately 3.11 Å based on covalent radius and bond length (Scheme 1(b)) [23–25], implying these nanopores will allow water molecules (kinetic diameter 2.6 Å [26]) to freely pass through. On the contrary, the molecules larger than the nanopores are expected to transport by longer and more tortuous paths due to the high aspect ratio of CNs. Thus the CNs may have molecular sieving function. Similar porous structures on graphene [27] and $g\text{-C}_3\text{N}_3$ nanosheets [28] have also found promising application potential for hydrogen (kinetic diameter 2.89 Å) purification. Additionally, CNs are usually synthesized by the thermal condensation method, which can generate defect-rich topological structure [21]. The planar structural defects with size of 3.1–3.4 Å are formed by the network terminations of uncondensed NH and NH_2 groups [29], enabling CNs more permeable to water. Owing to the unique structural characteristics, CNs may be ideal material for fabricating high-performance water-selective membranes. However, such utilizations of CNs have been rarely reported so far.

In the present study, CNs were synthesized and their topological and chemical structures were characterized. Sodium alginate (SA), a hydrophilic and widely used membrane material [30], was chosen as polymer matrix. The as-synthesized CNs were incorporated into SA matrix through physical blending method to prepare hybrid membranes. In order to understand the effect of the presence of CNs on the morphology, interfacial interactions, crystallinity, and hydrophilicity of the resultant hybrid membranes, systematic characterizations were performed. The water selective permeation behavior of the membranes was evaluated by pervaporation experiments using water/ethanol mixture as a model system. For comparison purpose, the hybrid membranes incorporated with nonporous (pore-blocked) CNs were prepared. Finally, the structural stability and long-term operating stability of the hybrid membranes were investigated as well.

2. Experimental

2.1. Materials

Sodium alginate (SA) was supplied by Qingdao Bright Moon seaweed Group Co. Ltd. (Shandong, China). Melamine, calcium chloride (CaCl_2), and absolute ethanol (≥ 99.7 wt%) were purchased from Tianjin Guangfu Technology Development Co. Ltd. (Tianjin, China). Polyacrylonitrile (PAN) ultrafiltration membranes with a molecular weight cut-off of 100,000 were obtained from Shandong MegaVision Membrane Engineering & Technology Co. Ltd. (Shandong, China). All reagents were of analytical grade and used without further purification. Deionized water was used throughout the experiments.

2.2. Synthesis of CNs

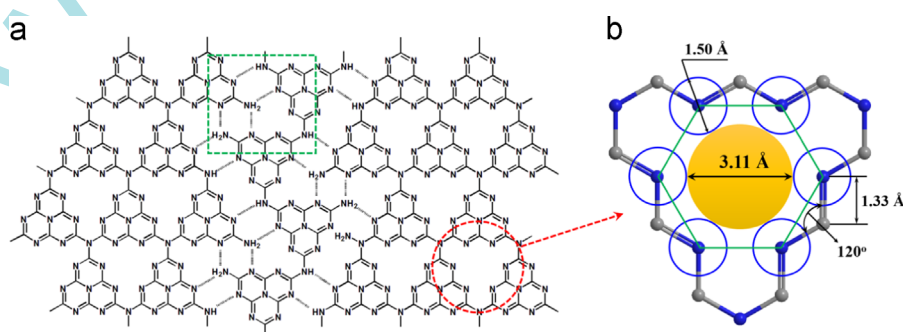
The CNs were synthesized by a novel route combining the thermal oxidation “etching” process [31] and ultrasound exfoliation [32]. In detail, melamine was heated at 550 °C for 4 h under air condition with a ramp rate of 3 °C/min for both heating and cooling processes. The resultant yellow product was milled into powder in a mortar. Then it was transferred into an open ceramic boat and heated at 500 °C in air for 2 h with a ramp rate of 5 °C/min. The obtained light yellow powder was dispersed in water with a concentration of 1 mg/ml. After ultrasonic treatment for about 6 h, the CNs were acquired by centrifugation.

2.3. Fabrication of membranes

The membranes were fabricated *via* physical blending. Certain amounts of CNs powders were dispersed into 25 ml water by sonication, followed by dissolving 0.38 g SA in above dispersions respectively with stirring for 5 h at 30 °C. The composite membranes were prepared by spin-coating each solution onto PAN substrates and removing the solvent under ambient conditions for 24 h. Thereafter, the membranes were cross-linked by immersing in 0.5 M CaCl_2 aqueous solution for 10 min, and were rinsed with abundant water. The hybrid membranes were denoted as SA-CN_s-X/PAN, where X varying from 1 to 5 represented the content of the CNs in SA (wt%). For characterization and swelling study, the free-standing membranes denoted as SA-CN_s-X were also fabricated following a similar preparation procedure.

2.4. Characterizations

The morphology of the CNs was observed by transmission electron microscopy (TEM, Tecnai G2 F20) and atomic force microscopy (AFM, CSPM5000), while that of the membranes was



Scheme 1. (a) Structural model of CNs with triangular nanopores in red circle and defects in green rectangle. (b) Structure magnification of the triangular nanopores. Grey spheres represent carbon atoms and blue spheres represent nitrogen atoms. The bond length of C–N is 1.33 Å and the bond angle of N–C–N is 120° [24]. The covalent diameter of nitrogen atom denoted by blue circle is 1.50 Å [25]. The geometric pore diameter can be derived as 3.11 Å.

characterized by field emission scanning electron microscopy (FESEM, Nanosem 430). The chemical structure of the nanosheets and membranes was characterized by Fourier transform infrared spectra (FT-IR, BRUKER Vertex 70 equipped with a horizontal attenuated total reflectance accessory) with a scan range of 4000–500 cm^{-1} and X-ray photoelectron spectroscopy (XPS, Perkin-Elmer PHI 1600 ESCA) with a monochromatic Mg $K\alpha$ source and a charge neutralizer. The crystalline structure of the nanosheets and membranes was investigated by X-ray diffraction (XRD, Rigaku D/max 2500 v/pc). The surface hydrophilicity of the membranes was probed by static contact angles (JC2000C Contact Angle Meter) on at least 6 different sites of each sample. Thermal gravimetric analysis (TGA, Netzsch 209 F3) and differential scanning calorimetry (DSC, Netzsch 204 F1) were conducted under nitrogen atmosphere to study the thermal behavior of the membranes. Mechanical property of the membranes was measured by an electronic stretching machine (Yangzhou Zhongke WDW-02) at a strain rate of 2 mm/min.

2.5. Swelling and separation experiments

The dry free-standing membranes were weighed (W_D) in advance. After soaking in 90 wt% ethanol aqueous solution at 76 °C for 48 h, the swollen membranes were reweighed (W_S) after quickly removing the surface liquid. The swelling degree (SD, %) was calculated by

$$SD = \frac{W_S - W_D}{W_D} \times 100 \quad (1)$$

The separation equipment was described previously [33]. Feed was circulated at a flow rate of 60 L/h under normal pressure, and the pressure of permeate side was below 0.3 kPa. The effective area of membrane was 25.6 cm^2 . The permeate was collected by a liquid nitrogen cold trap and analyzed by gas chromatography (HP 4890). The permeation flux (J , $\text{kg}/(\text{m}^2 \text{h})$) and separation factor (α) were calculated as

$$J = \frac{Q}{At} \quad (2)$$

$$\alpha = \frac{P_W/P_E}{F_W/F_E} \quad (3)$$

where Q (g) is the mass of the permeate during operation time t (h), and A (m^2) is the effective membrane area. P and F are the

mass fractions of water (W) or ethanol (E) in permeate and feed, respectively.

Moreover, the permeance ($(P/l)_i$, GPU, 1 GPU = $7.501 \times 10^{-12} \text{ m}^3$ (STP)/ $\text{m}^2 \text{ s Pa}$) and selectivity (β) were calculated by following equations to decouple the effect of driving forces [34]:

$$(P/l)_i = \frac{J_i}{p_{i0} - p_{il}} = \frac{J_i}{\gamma_{i0} \chi_{i0} p_{i0}^{\text{sat}} - p_{il}} \quad (4)$$

$$\beta = \frac{(P/l)_W}{(P/l)_E} \quad (5)$$

where l (m) is the thickness of membrane; J_i ($\text{g}/(\text{m}^2 \text{ h})$) is the permeation flux of component i ; p_{i0} (Pa) and p_{il} (Pa) are the partial pressures of component i on the feed and permeate side; γ_{i0} and χ_{i0} are the activity coefficient and mole fraction of component i in feed; p_{i0}^{sat} (Pa) is the saturated vapor pressure of pure component i . The permeation flux (P) of each component is transformed into the volumes under standard temperature and pressure (STP).

3. Results and discussion

3.1. Characterization of CNs

The morphology of CNs was investigated by TEM and AFM. As clearly observed in Fig. 1(a), CNs showed a graphene-like 2D morphology with many wrinkles and grooves. The ultrathin 2D structure was further probed by AFM. Fig. 1(b) revealed the lateral size of the as-obtained sample was around several microns, and the thickness was approximately 0.96 nm. It is obvious that the ultrathin CNs was successfully synthesized by the combination of thermal oxidation etching and liquid exfoliation approaches.

To explore the crystalline structure of CNs, XRD was conducted and the result was shown in Fig. 2(a). Two characteristic diffraction peaks were observed in the XRD pattern of CNs. The strong peak located at 27.1° corresponded to the stacking of conjugated aromatic (0 0 2) planes with the d -spacing of 0.329 nm. Besides, the relatively weak peak at 12.5° ($d=0.710$ nm) was assigned to in-plane structural packing motif of tri-s-triazine units, as the size of one such unit is about 0.713 nm [35], which indicated the as-synthesized CNs possessed triangular nanopores within tri-s-triazine building units.

Furthermore, the nanoporous structure of CNs including triangular nanopores and structural defects were probed by FT-IR. As

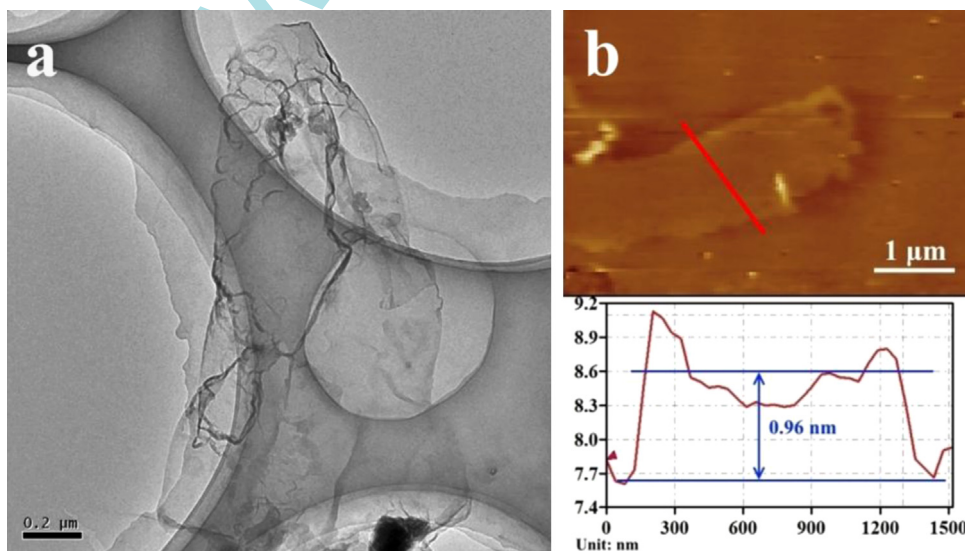


Fig. 1. (a) TEM image and (b) AFM images of CNs.

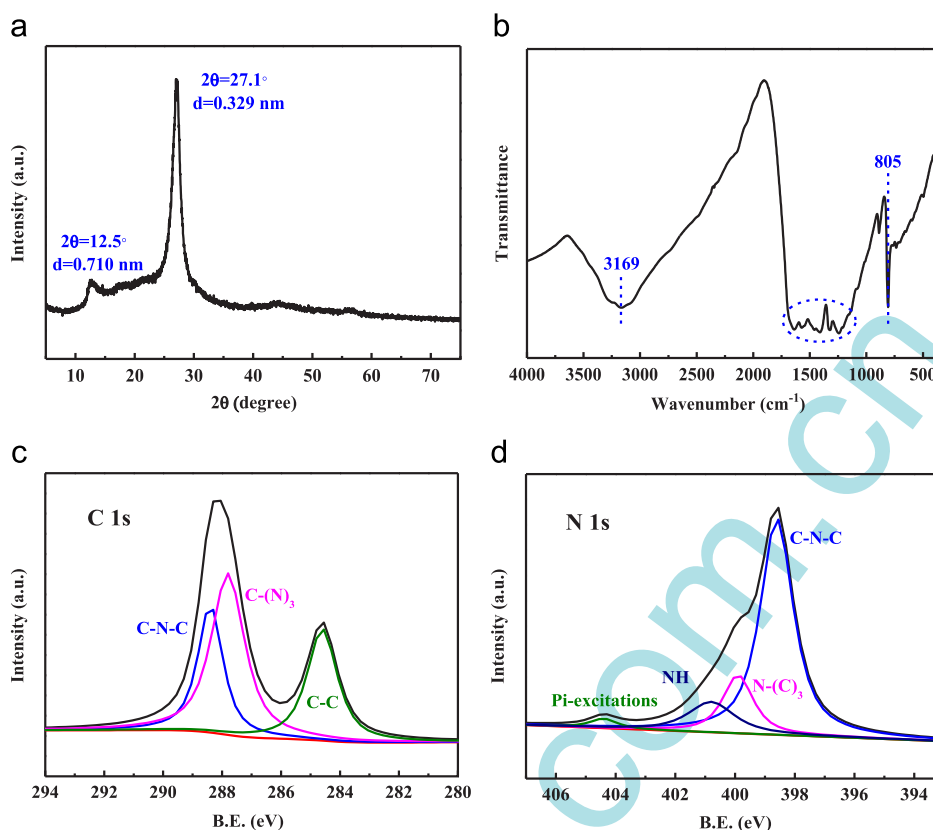


Fig. 2. (a) XRD pattern, (b) FT-IR spectrum, (c) high-resolution C 1s spectra, and (d) high-resolution N 1s spectra of CNs.

depicted in Fig. 2(b), the spectrum of CNs exhibited a sharp peak at 805 cm^{-1} , which originated from the out-of-plane bending vibration of tri-s-triazine ring system [31]. Accordingly, the existence of triangular nanopores in CNs was further confirmed. Several strong absorption bands in the region of $1200\text{--}1650\text{ cm}^{-1}$ corresponded to the typical stretching modes of either trigonal $\text{N}-(\text{C})_3$ (full condensation) or bridging C-NH-C (partial condensation) units [29]. A shoulder band near 3169 cm^{-1} was contributed by the terminal NH or NH_2 groups at the defect sites of the aromatic ring [36], indicating the presence of partially condensed network and structural defects [29].

The structure information of CNs was further acquired by XPS measurement. The high resolution C 1s spectra in Fig. 2(c) could be deconvoluted into three peaks at binding energies of 288.4, 287.8 and 284.6 eV, where the former two peaks represented the sp^2 C atoms bonded to N and the latter peak was related to surface adventitious carbon [37]. Besides, as revealed by the N 1s high resolution XPS spectrum in Fig. 2(d), the peak at 398.6 eV was attributed to sp^2 hybridized N atoms in aromatic rings (C-N-C), while the peaks at 399.9, 400.8, and 404.4 eV were assigned to tertiary N atoms in $\text{N}-(\text{C})_3$, the terminal amino groups (NH) [38], and pi-excitations [37], respectively.

3.2. Morphology of the membranes

SEM was employed to assess the morphology of the hybrid membranes as well as the pure SA membrane. As shown in Fig. 3 (a–d), all the active layers were dense and uniform with an average thickness of approximately $0.5\text{ }\mu\text{m}$, and tightly adhered to the porous PAN substrates. Unlike the smooth morphology of pure SA active layer (Fig. 3(a)), there were some visible nanosheets dispersed in the active layers of hybrid membranes (Fig. 3(b–d)). The presence of CNs was further confirmed by the comparison of surface morphology of the pure SA membrane (Fig. 3(e)) and

hybrid membranes (Fig. 3(f–h)). Moreover, as the CNs content increased, partial agglomeration of CNs presented in the surface of SA-CNs-3/PAN (Fig. 3(g)), and it became more pronounced in SA-CNs-5/PAN (Fig. 3(h)). To gain more insight into the dispersion state of CNs in SA matrix, cross-section images of the free-standing membranes were shown in Fig. 4. The pure SA membrane displayed typically smooth morphology (Fig. 4(a)), while Fig. 4 (b) shows homogenous dispersion of CNs. Most of the CNs exhibited preferential orientations paralleled with membrane surface, which was a spontaneous behavior of the 2D fillers in hybrid membranes [39]. Upon increasing CNs content, the cross-section of SA-CNs-3 (Fig. 4(c)) demonstrated well-aligned lamellar structure. However, as revealed in Fig. 4(d), the alignment of CNs became somewhat disordered, which was probably ascribed to the surface activation energy that forced some adjacent nanosheets to restack together into agglomerates. Such phenomena were also observed in other reported hybrid membranes [40,41].

3.3. Interfacial interactions in the membranes

FT-IR is a vital tool to determine interfacial interactions between CNs and SA matrix. As shown in Fig. 5(a), the characteristic bands at 3349.2 cm^{-1} in the spectrum of pure SA membrane corresponded to the OH stretching vibration of hydroxyl group, while the absorption bands at 1606.3 and 1430.2 cm^{-1} originated from the COO^- symmetric and asymmetric stretching vibration of carboxylate salt [42]. However, after the incorporation of CNs, all the three characteristic bands in SA obviously shifted to lower wavenumbers compared with those of the pure SA membrane. In the meantime, the intensity of these bands gradually declined with increasing CNs content. The peak position shift and relative intensity change suggested the formation of strong interfacial interactions, mainly resulting from the intermolecular hydrogen

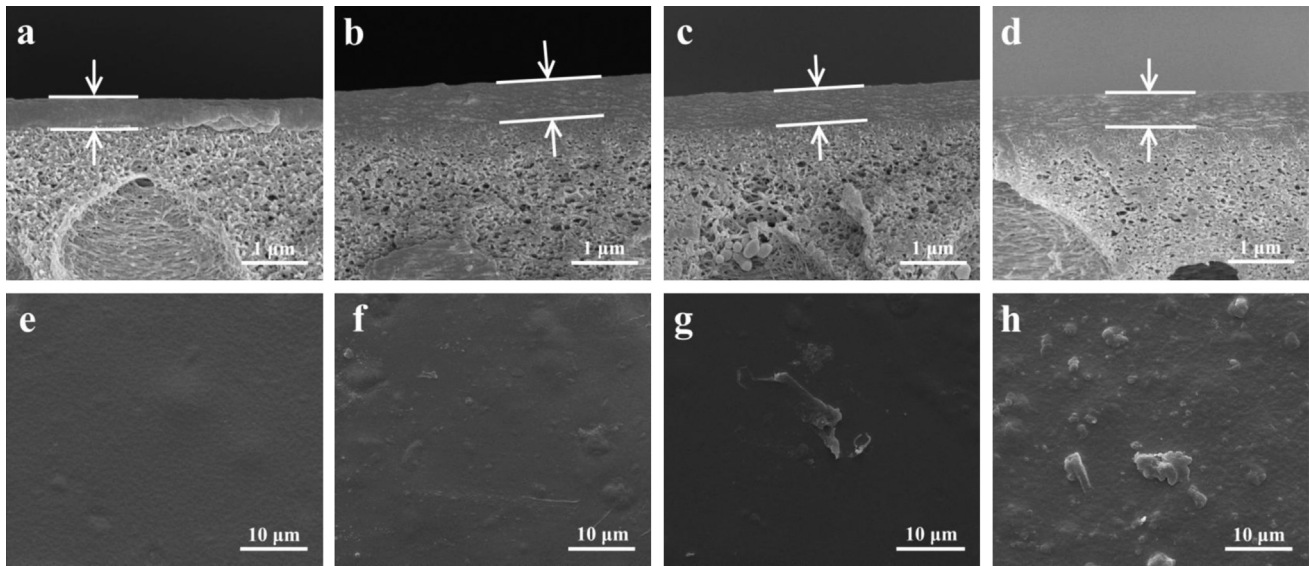


Fig. 3. SEM cross-section images of (a) SA pure/PAN, (b) SA-CNs-2/PAN, (c) SA-CNs-3/PAN, (d) SA-CNs-5/PAN. SEM surface images of (e) SA pure/PAN, (f) SA-CNs-2/PAN, (g) SA-CNs-3/PAN, and (h) SA-CNs-5/PAN.

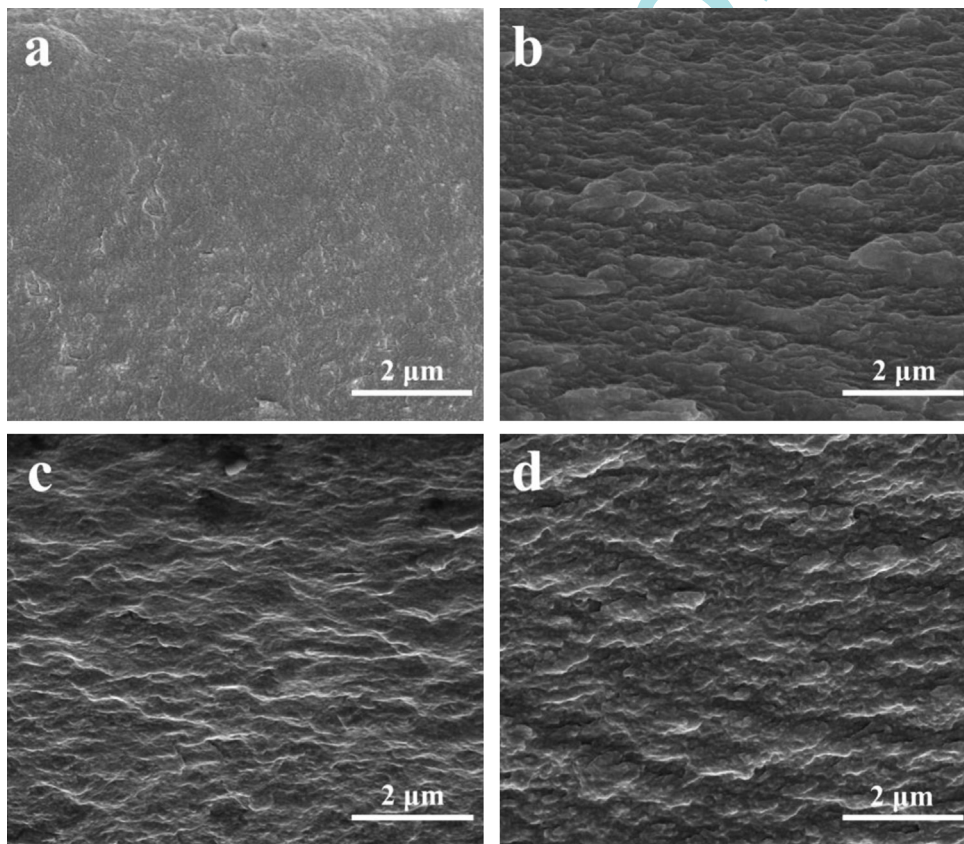


Fig. 4. SEM cross-section images of (a) SA pure, (b) SA-CNs-2, (c) SA-CNs-3, and (d) SA-CNs-5.

bonds between the residual NH or NH₂ groups of CNs and the OH or COO⁻ groups of SA chains [43].

The interfacial interactions in membranes could also be inferred by their mechanical property. As described in Fig. 5(b), with increasing CNs content from 1 to 2 wt%, both the tensile strength and tensile modulus of hybrid membranes were enhanced compared with those of the pure SA membrane, and then decreased as the CNs content further increased. The tensile strength of SA-CNs-2 increased by 27% from 85.8 to 108.9 MPa,

and its tensile modulus increased by 100% from 2.29 to 4.60 GPa. The reinforcement was mainly attributed to the homogeneous dispersion of CNs in the membranes and strong interfacial interactions between CNs and SA chains [40,44]. When the CNs content exceeded 2 wt%, the mechanical property started deteriorating, which was probably caused by the agglomeration of CNs [44]. It is worth mentioning that the tensile modulus of the hybrid membranes was still higher than that of pure SA membrane even at high CNs content.

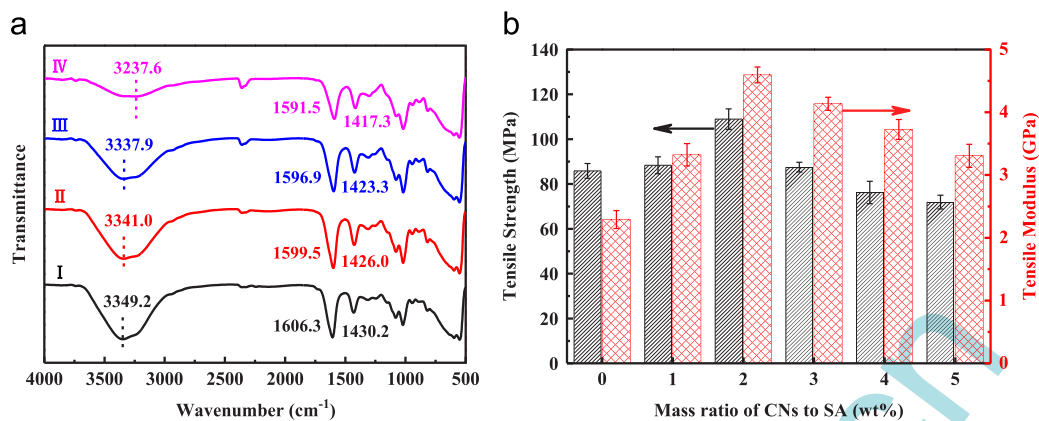


Fig. 5. (a) FT-IR spectra of (I) SA pure/PAN (II) SA-CNs-2/PAN, (III) SA-CNs-3/PAN, and (IV) SA-CNs-5/PAN. (b) Tensile strength and tensile modulus of the membranes with different CNs contents.

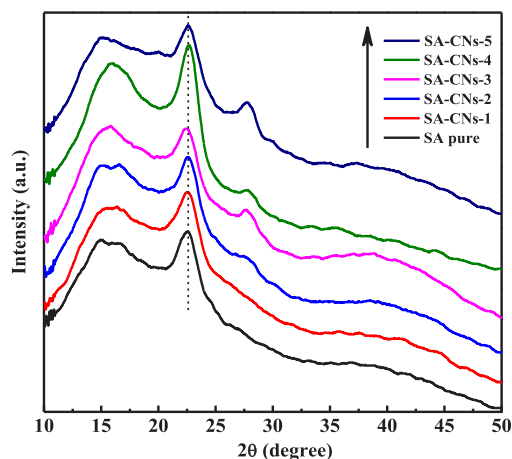


Fig. 6. XRD patterns of the membranes with different CNs contents.

3.4. Crystallinity of the membranes

As for semi-crystalline polymers, like SA, it is believed that only the amorphous phase is permeable for molecules, while the crystalline regions are impermeable barriers [45]. The crystallinity of the membranes was therefore evaluated by XRD analysis. As depicted in Fig. 6, the characteristic peak of CNs ($2\theta=27.1^\circ$) was undetectable in the XRD patterns of SA-CNs-1 and SA-CNs-2, indicating the effective exfoliation and homogeneous dispersion of CNs in SA matrix. When CNs content exceeded 2 wt%, the peak at $2\theta=27.1^\circ$ appeared with increasing intensity, further confirming the agglomeration of CNs. All the membranes showed two characteristic peaks: the sharp peak at $2\theta=23^\circ$ associating with crystalline region and the broad peak at $2\theta=15^\circ$ belonging to amorphous nature. The intensity of crystalline peak ($2\theta=23^\circ$) decreased gradually with increasing CNs content (lower than 4 wt%), then dramatically increased for SA-CNs-4, and finally decreased again for SA-CNs-5. This change trend was further confirmed by the weight-averaged crystallinity of different membranes listed in Table 1. The crystallinity of the membranes could be affected by three aspects: (1) the interfacial interactions could disrupt the ordered SA chain packing and induce more amorphous regions and larger interchain spacing, thus decreasing the crystallinity; (2) CNs could act as nucleating agents leading to higher crystallinity; (3) the agglomeration of CNs at high content weakened the nucleating effect, which decreased the crystallinity. The decrease of crystallinity at low CNs contents was mainly due to the interfacial interactions, while the nucleating effect became more dominant that increased the crystallinity of SA-CNs-4. Agglomeration of CNs caused the decline of crystallinity of

Table 1

Weight-averaged crystallinity of the membranes with different CNs contents.

Membrane	Weight-averaged crystallinity (%)
SA pure	12.69
SA-CNs-1	11.43
SA-CNs-2	9.06
SA-CNs-3	7.90
SA-CNs-4	13.51
SA-CNs-5	12.06

SA-CNs-5 [40]. Similar tendencies were also found in our previous study [16].

3.5. Thermal property of the membranes

TGA was employed to characterize the thermal stability of the pure SA membrane and hybrid membranes. As revealed in Fig. 7 (a), three stages are visible in the process of thermal weight loss: the first stage under 215°C corresponding to the traces of moisture, the second stage between 215 and 400°C corresponding to the decomposition of functional groups in SA, and the third stage in the range from 400 to 700°C corresponding to the degradation of the SA backbone. These results indicated that all the hybrid membranes were thermally stable below 215°C , which was satisfactory for pervaporation operation.

In order to investigate the chain mobility and chain rigidity of SA matrix, the glass transition temperature (T_g) of the membranes was estimated by DSC. As shown in Fig. 7(b), T_g remained nearly unchanged upon the increase of CNs content. On one hand, the inclusion of CNs could disrupt the inherent compactness of SA chains and enhanced the chain flexibility [46]. On the other hand, the effective attachment of SA to the CNs could restrict the segmental motion of the SA chains [43]. These opposite effects could account for the preserved rigidity of SA chains.

3.6. Hydrophilicity and swelling property of the membranes

Since the surface hydrophilicity is a crucial factor for water-selective membranes, water contact angles of the membranes were measured. Fig. 8(a) shows that the pure SA membrane had the lowest contact angle of 29.6° due to the high hydrophilicity of SA. The hybrid membranes exhibited slightly higher contact angles due to the less hydrophilic groups on CNs. Yet the hydrophilicity of hybrid membranes was still strong enough (contact angles were all lower than 37°) for potential water separation.

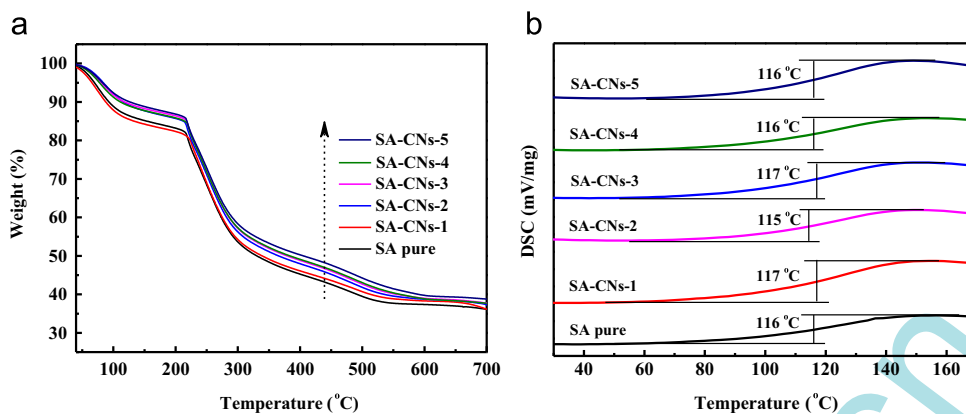


Fig. 7. (a) TGA curves and (b) DSC traces of the membranes with different CNs contents.

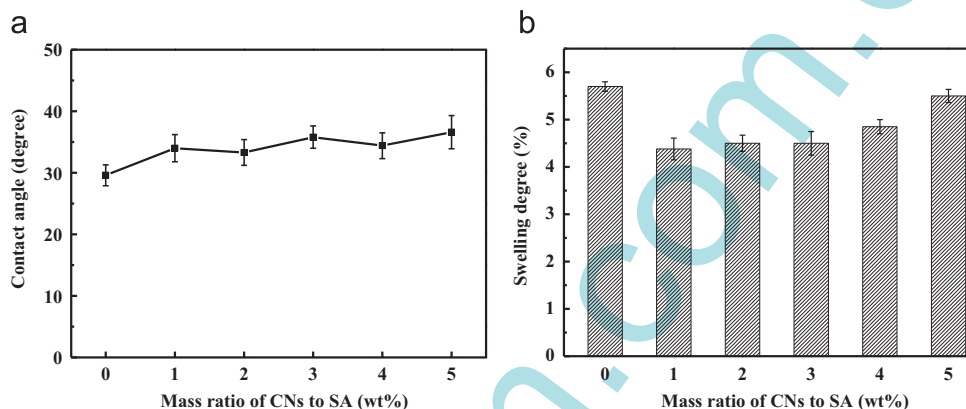


Fig. 8. (a) Contact angle and (b) swelling degree of the membranes with different CNs contents.

To determine the effect of CNs on swelling behavior of the hybrid membranes, swelling degree of the membranes was tested and shown in Fig. 8(b). In contrast to SA pure membrane, all the hybrid membranes exhibited lower swelling degree. The possible reason might be that the interfacial interactions between the SA matrix and CNs could effectively hinder the stretching of the SA chains in aqueous solution [44]. At higher CNs contents (4 and 5 wt%), the increase of swelling degree was mainly ascribed to the agglomeration of CNs [16].

3.7. Separation performance of the membranes

To investigate the effect of CNs on permeability and selectivity of the membranes, pervaporation separation of 90 wt% water/ethanol mixtures was conducted at 76 °C. As shown in Fig. 9, both the permeation flux and separation factor of the hybrid membranes enhanced significantly by incorporating up to 3 wt% CNs, which suggested the successful breakthrough of tradeoff tether. Since the surface hydrophilicity of hybrid membranes decreased slightly (Fig. 8(a)), the remarkable enhancement of separation performance was primarily attributed to the structural change of SA matrix and the inherent properties of CNs. Fig. 6 confirmed that the inclusion of CNs disrupted the SA chain compactness and increased the amorphous dominants and interchain spacing, when the CNs content did not exceed 3 wt%. In consequence, SA matrix became more permeable to both water and ethanol, resulting in the enhancement of permeation flux. In general, decreased crystallinity could induce the sacrifice of selectivity, because the permeation of larger molecules was more sensitive to the enlargement of interchain spacing. Nevertheless, the change of separation factor was just opposite, and the sieving effect of CNs was believed

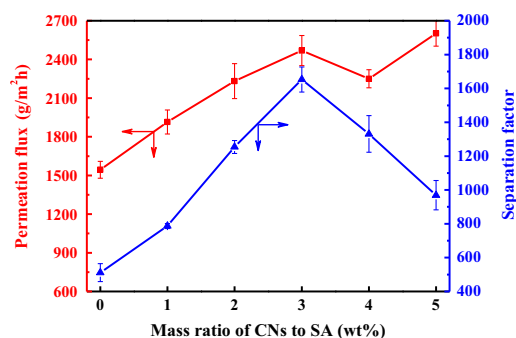
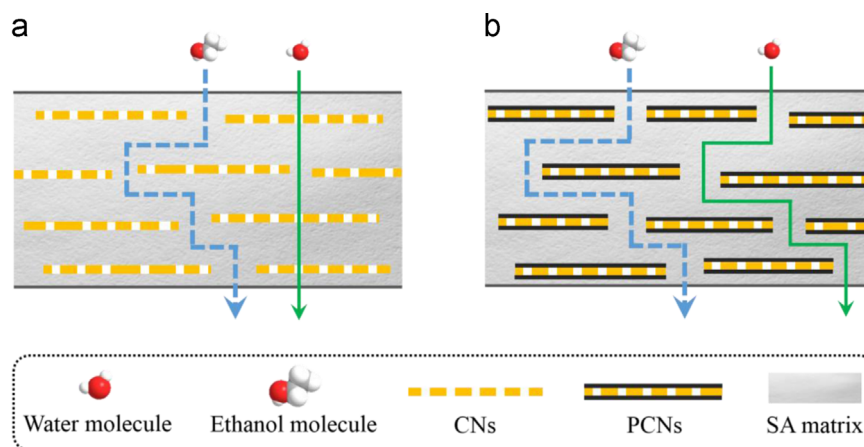


Fig. 9. Separation performance of the membranes with different CNs contents.

to be responsible for the improved selectivity. As shown in Scheme 2(a), the horizontally lamellar structure (Fig. 4(b and c)) necessitated longer and more tortuous paths for ethanol molecules, which cannot easily pass through the nanopores on CNs as the kinetic diameter of ethanol molecules (4.5 Å) is larger than the size of nanopores (3.1–3.4 Å). On the contrary, the appropriate nanopore size and small thickness of CNs allowed fast permeation of water molecules [47]. As a result, the separation factor was improved. High separation performance with a permeation flux of 2469 g/m² h and a separation factor of 1653 was achieved for hybrid membrane incorporated with 3 wt% CNs. With further increasing of CNs content, the separation factor decreased due to the weakened sieving effect causing by disordered structure (Fig. 4(d)). The permeation flux decreased for SA-CNs-4/PAN, and then increased again for SA-CNs-5/PAN, which was in consistent with the tendency of crystallinity revealed in Fig. 6.



Scheme 2. Schematic diagrams of molecular transport through hybrid membranes incorporating horizontally aligned (a) CNs and (b) polydopamine-coated $g\text{-C}_3\text{N}_4$ nanosheets (PCNs).

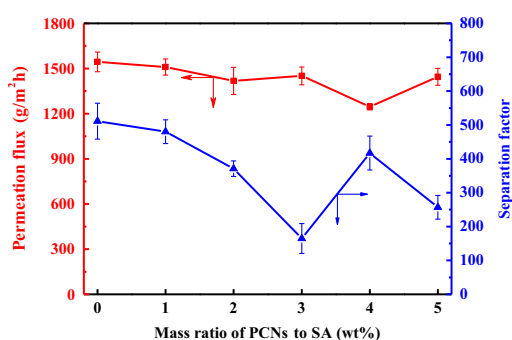


Fig. 10. Separation performance of the membranes with different PCNs contents.

To further identify the sieving effect of CNs, polydopamine-coated $g\text{-C}_3\text{N}_4$ nanosheets (PCNs) was synthesized and incorporated into SA matrix to prepare hybrid membranes (Supplementary material). As is well known, dopamine can perform oxidation, self-polymerization, and aggregation to form a polydopamine coating layer with controllable thickness on diverse surfaces [48]. It has been found that the polydopamine coating could induce pore-blocking that impeded water permeation through membranes [49,50]. As demonstrated by results of TEM, XRD and FT-IR (Figs. S1(a) and S2(a and b) (Supplementary material)), PCNs exhibited similar ultrathin 2D morphology, crystalline and chemical structure to those of CNs. Meanwhile, the changes in thickness, thermal property, and color (Figs. S1(b) and S2(c and d) (Supplementary material)) suggested the successful coating of polydopamine layer on PCNs. As shown in Fig. 10, the separation factor decreased significantly with increasing PCNs content (1–3 wt%), while the permeation flux only slightly declined. As the PCNs-incorporated membranes exhibited similar surface and cross-section morphology, characteristic FI-IR bands shift, crystallinity change trend, and surface hydrophilicity (Figs. S3, S4(a), S5 and S6 (a) (Supplementary material)) to those of CNs-incorporated membranes, the different effects of CNs and PCNs on separation performance could be ascribed to their different nanoporous structures. As shown in Scheme 2(b), because the nanopores on nanosheets were blocked by the polydopamine layer, both water molecules and ethanol molecules could hardly pass through the PCNs, which markedly decreased the permeation flux and weakened their contributions to separation selectivity. Moreover, Figs. S4(b) and S6(b) (Supplementary material) indicated the hybrid membranes with PCNs content less than 3 wt% had stronger interfacial interactions than those of CNs-incorporated membranes, leading to more significant enlargement of interchain

spacing. In other words, SA matrix became more permeable and less selective. Hence, as shown in Fig. 10, the separation factor decreased for the membranes with less than 3 wt% PCNs. The slight decrease of the permeation flux was ascribed to the more pronounced impeding effect of PCNs. A typical tradeoff phenomenon was observed with further increasing PCNs content, which could be explained by the increased crystallinity of SA-PCNs-4 and decreased crystallinity of SA-PCNs-5 (Fig. S5 (Supplementary material)). This contrast experiment verified the sieving effect of CNs was arisen from their nanoporous structure.

3.8. Effect of feed temperature and feed concentration on separation performance

Considering the vibrations of operating conditions in practical application, it is necessary to examine the separation performances at varied feed temperatures and feed concentrations. Fig. 11(a–c) depicted the permeation fluxes, separation factor, permeance, and selectivity versus feed temperature of SA-CNs-3/PAN for 90 wt% ethanol/water mixture. As the temperature increased, the total flux increased continuously (Fig. 11(a)) as well as water and ethanol fluxes (Fig. 11(b)), which was mainly derived from three reasons: the enhanced the driving forces [51], the increased the fractional free volume within membranes [52], and the higher molecular diffusivity [53]. As revealed in Fig. 11(c), water permeance increased monotonically, while ethanol permeance decreased over the temperature range 40–70 °C, resulting in the elevation of selectivity. According to solution-diffusion mechanism, the molecular transport was controlled by the sorption process at membrane surface and diffusion process across membrane. Because the membranes were rather hydrophilic (Fig. 8(a)), the weakened effect of raised temperature on sorption for ethanol was greater than that for water [54]. The sorption process might be more dominant to cause more pronounced amplitude of ethanol solubility decrement than its diffusivity increment, since the driving force has been normalized. Similarly, water flux increased more prominently than ethanol flux, which led to the increase of separation factor (Fig. 11(a), 40–70 °C). The different behaviors of water flux and ethanol flux with increased temperature were further indicated by the Arrhenius equation [55]

$$J = A_0 \exp\left(-\frac{E_p}{RT}\right) \quad (6)$$

where J , A_0 , E_p , R and T are the permeation flux, pre-exponential factor, apparent activation energy, gas constant, and feed temperature, respectively. The curve was well fitted in Fig. 11(d), and

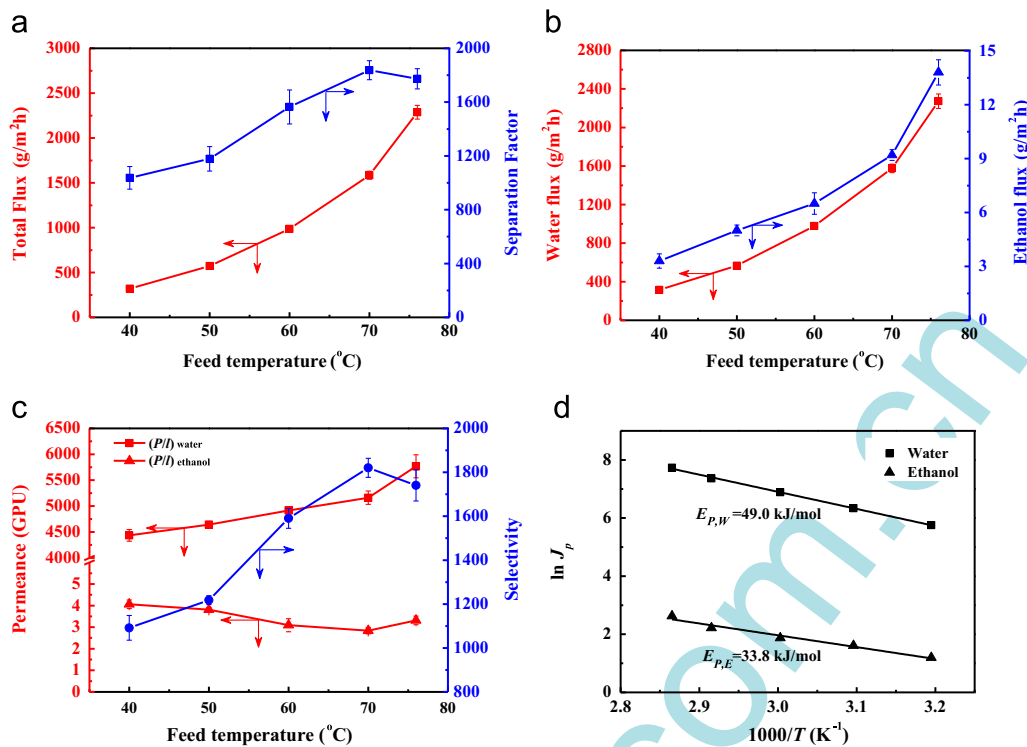


Fig. 11. Effect of feed temperature on (a) total flux and separation factor, (b) water flux and ethanol flux, and (c) permeance and selectivity of SA-CNs-3/PAN for the dehydration of 10 wt% water/ethanol mixtures. (d) Arrhenius plots of water and ethanol fluxes.

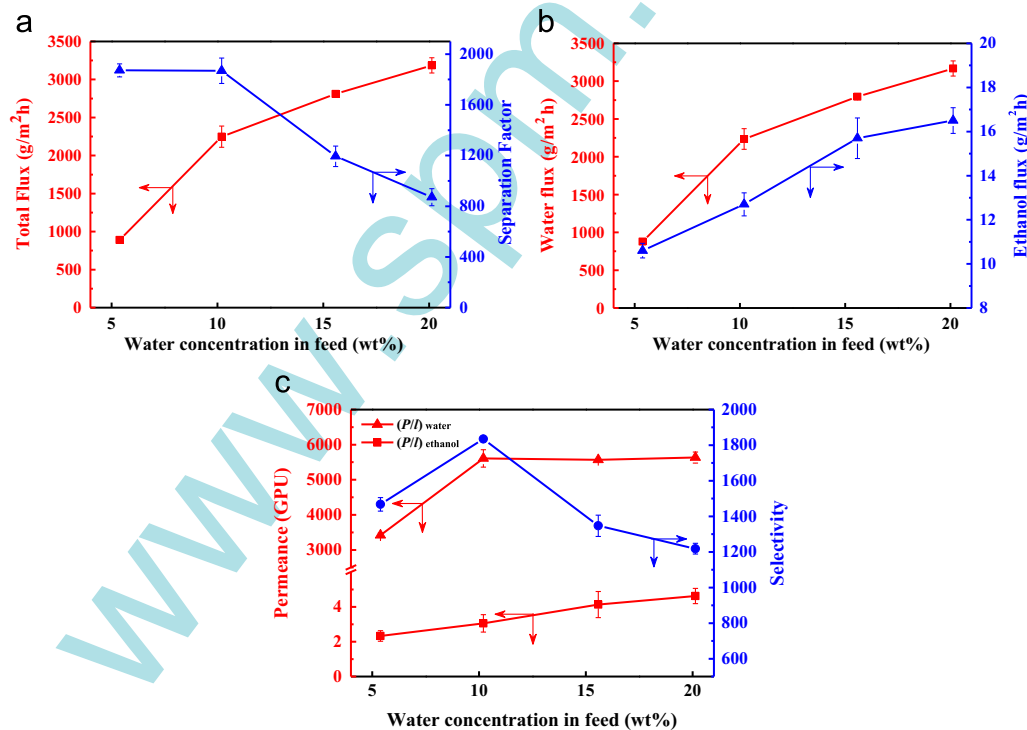


Fig. 12. Effect of water concentration in feed on the (a) total flux and separation factor, (b) water flux and ethanol flux, and (c) permeance and selectivity of SA-CNs-3/PAN for the dehydration of water/ethanol mixtures at 76 °C.

the apparent activation energy of water and ethanol were 49.0 kJ/mol and 33.8 kJ/mol, respectively. The higher activation energy of water suggested that the permeation of water was more sensitive to temperature changes, that is to say water flux increased more quickly than ethanol flux with increased temperature [56]. At higher feed temperature, the expansion of free

volume in membrane was more favorable to the transfer of ethanol molecules with larger kinetic radii. Thus, ethanol permeance was supposed to increase at 76 °C, leading to the decline of selectivity and separation factor.

As shown in Fig. 12(a), with increasing water concentration in feed at 76 °C, the total flux of SA-CNs-3/PAN increased, while the

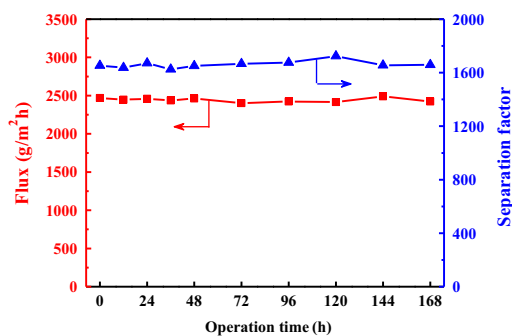


Fig. 13. Long-term operating stability of SA-CNs-3/PAN for the dehydration of 10 wt% water/ethanol mixture at 76 °C.

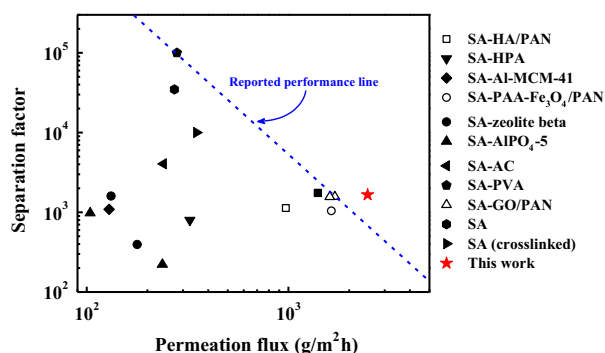


Fig. 14. Separation performance for ethanol dehydration as reported in literatures and in this work. Membranes reported in previous studies: SA-HA/PAN (HA: hyaluronic acid) [59]; SA-HPA (HPA: type heteropolyacid $H_{14}[NaP_5W_{30}O_{110}]$) [60]; SA-Al-MCM-41 (Al-MCM-41: aluminum-containing mesoporous silica) [61]; SA-PAA- Fe_3O_4 /PAN (PAA: Poly(acrylic acid)) [62]; SA-zeolite beta [63]; SA- $AlPO_4-5$ ($AlPO_4-5$: microporous aluminophosphate) [64]; SA-PVA (PVA: poly(vinyl alcohol)) [65]; SA-GO-PAN (GO: pristine graphene oxide or reduced graphene oxide) [16]; SA [66]; SA (crosslinked) [67].

separation factor decreased. This trend could be explained by the joint effects of membrane swelling and driving forces [57]. As water concentration increased in feed, the enhanced swelling effect tended to increase the free volume in membrane, facilitating both the water and ethanol transport. In the meantime, increased water concentration could also enhance the driving forces for water and reduce those for ethanol [58]. Therefore, water flux increased. And the increased ethanol flux (Fig. 12(b)) was probably because the positive swelling effect on ethanol permeation was more significant than the negative driving forces effect. The ethanol permeance increased with increasing water concentration (Fig. 12(c)), further confirming the swelling contribution. At low water concentration (10 wt%), the membrane was only moderately swollen, resulting in the increase of water permeance. With further increasing water concentration, more and larger water clusters were formed, hindering the water permeation. The effect of water clusters might be offset by membrane swelling, so that the water permeance remained almost constant upon water concentration ranging from 10 to 20 wt%. Hence, the selectivity increased at first then declined with increasing water concentration in feed.

3.9. Long-term operating stability of the membrane

Long-term stability of membrane during operation is critical for practical applications. The long-term separation performance of SA-CNs-3/PAN for 90 wt% ethanol/water mixture at 76 °C was examined and shown in Fig. 13. Both the permeation flux and

separation factor remained stable in a run up to 120 h. It was the good thermal and mechanical stability as well as the enhanced swelling resistance that endowed the membrane with desirable long-term stability.

3.10. Comparison of separation performance with SA-based membranes

Fig. 14 shows a comparison of separation performance for ethanol dehydration between membrane in this work and SA-based membranes in literatures. It can be found that the SA-CNs-3/PAN exhibited an extremely high permeation flux, which was 45.3% more than the optimized value achieved in our previous study [16], as well as an acceptable separation factor. The performance of SA-CNs-3/PAN clearly transcended the upper bound of the state-of-the-art SA-based membranes.

4. Conclusion

This study demonstrated that high-performance water-selective membranes could be prepared by physically blending CNs into SA matrix. Through thermal oxidation “etching” and ultrasound exfoliation procedures, CNs with ultrathin 2D morphology and nanoporous structures were synthesized. In the hybrid membranes, CNs played the following three major roles: (1) CNs formed horizontal alignment within the hybrid membranes, constructing ordered channels for water transport due to their ultrathin 2D morphology and high aspect ratio; (2) the nanoporous structure of CNs offered molecular sieving effect, facilitating the preferential permeation of water molecules over ethanol molecules and thus leading to high selectivity; (3) interfacial interactions arisen from the hydrogen bonds between residual NH or NH_2 groups of CNs and OH or COO^- groups of SA chains decreased the crystallinity of polymer matrix and enhanced the permeation flux. Consequently, the hybrid membrane with the CNs content of 3 wt% exhibited an optimal pervaporation performance with a permeation flux of $2469 \text{ g/m}^2 \text{ h}$ and a separation factor of 1653 for the dehydration of 10 wt% water/ethanol mixture at 76 °C, which was quite high compared with those of other SA-based membranes in literatures. Furthermore, the hybrid membranes displayed good mechanical, thermal, and anti-swelling properties, ensuring the practical operations under different conditions and long timespan. Due to the unique topological and chemical structures as well as easy mass-production of CNs, membranes incorporated with CNs may find promising applications in water treatment and separation of small molecule mixtures.

Acknowledgements

This work was financially supported by the National Science Fund for Distinguished Young Scholars (No. 21125627), the National Natural Science Foundation of China (No. 21490583), the National Natural Science Foundation of China (No. 21306131), the Specialized Research Fund for the Doctoral Program of Higher Education (20120032120009), and the State Key Laboratory of Chemical Engineering (No. SKL-ChE-13B03).

Appendix A. Supplementary material

Supplementary data associated with this article can be found in the online version at <http://dx.doi.org/10.1016/j.memsci.2015.04.050>.

Nomenclature

Symbols

<i>A</i>	effective membrane area (m ²)
<i>E</i>	apparent activation energy (kJ/mol)
<i>F</i>	mass fraction in feed solution (wt%)
<i>J</i>	permeation flux (g/m ² h)
<i>l</i>	membrane thickness (m)
<i>P</i>	mass fraction in permeate solution (wt%)
<i>p</i> ₀	partial pressure in the feed side (kPa)
<i>p</i> ₁	partial pressure in the permeate side (kPa)
<i>P</i> / <i>l</i>	permeance (GPU)
<i>Q</i>	mass of permeate (g)
<i>W</i>	mass of membrane (g)
<i>X</i>	CNs content in hybrid membrane (wt%)

Greek letters

α	separation factor
β	selectivity
γ	activity coefficient
χ	mole fraction

Subscripts

<i>D</i>	dry membrane
<i>E</i>	ethanol
<i>S</i>	swollen membrane
<i>W</i>	water

Abbreviations

CNs	g-C ₃ N ₄ nanosheets
PAN	polyacrylonitrile
PCNs	polydopamine-coated g-C ₃ N ₄ nanosheets
SA	sodium alginate
SD	swelling degree (%)

References

- [1] M.A. Shannon, P.W. Bohn, M. Elimelech, J.G. Georgiadis, B.J. Marinas, A. M. Mayes, Science and technology for water purification in the coming decades, *Nature* 452 (2008) 301–310.
- [2] Q. Zhao, Q.F.F. An, Y.L. Ji, J.W. Qian, C.J. Gao, Polyelectrolyte complex membranes for pervaporation, nanofiltration and fuel cell applications, *J. Membr. Sci.* 379 (2011) 19–45.
- [3] V.T. Magalad, G.S. Gokavi, M.N. Nadagouda, T.M. Aminabhavi, Pervaporation separation of water-ethanol mixtures using organic-inorganic nanocomposite membranes, *J. Phys. Chem. C* 115 (2011) 14731–14744.
- [4] G.M. Geise, H.B. Park, A.C. Sagle, B.D. Freeman, J.E. McGrath, Water permeability and water/salt selectivity tradeoff in polymers for desalination, *J. Membr. Sci.* 369 (2011) 130–138.
- [5] B. Bolto, M. Hoang, Z. Xie, A review of membrane selection for the dehydration of aqueous ethanol by pervaporation, *Chem. Eng. Process.* 50 (2011) 227–235.
- [6] B.D. Freeman, Basis of permeability/selectivity tradeoff relations in polymeric gas separation membranes, *Macromolecules* 32 (1999) 375–380.
- [7] G.M. Geise, D.R. Paul, B.D. Freeman, Fundamental water and salt transport properties of polymeric materials, *Prog. Polym. Sci.* 39 (2014) 1–42.
- [8] R.R. Nair, H.A. Wu, P.N. Jayaram, I.V. Grigorieva, A.K. Geim, Unimpeded permeation of water through helium-leak-tight graphene-based membranes, *Science* 335 (2012) 442–444.
- [9] Y. Han, Z. Xu, C. Gao, Ultrathin graphene nanofiltration membrane for water purification, *Adv. Funct. Mater.* 23 (2013) 3693–3700.
- [10] M. Hu, B. Mi, Enabling graphene oxide nanosheets as water separation membranes, *Environ. Sci. Technol.* 47 (2013) 3715–3723.
- [11] R.K. Joshi, P. Carbone, F.C. Wang, V.G. Kravets, Y. Su, I.V. Grigorieva, H.A. Wu, A. K. Geim, R.R. Nair, Precise and ultrafast molecular sieving through graphene oxide membranes, *Science* 343 (2014) 752–754.
- [12] W. Hung, C. Tsou, M. De Guzman, Q. An, Y. Liu, Y. Zhang, C. Hu, K. Lee, J. Lai, Cross-linking with diamine monomers to prepare composite graphene oxide-framework membranes with varying d-spacing, *Chem. Mater.* 26 (2014) 2983–2990.
- [13] K. Huang, G. Liu, Y. Lou, Z. Dong, J. Shen, W. Jin, A graphene oxide membrane with highly selective molecular separation of aqueous organic solution, *Angew. Chem.-Int. Ed.* 53 (2014) 6929–6932.
- [14] S.P. Dharupaneedi, R.V. Anjanapura, J.M. Han, T.M. Aminabhavi, Functionalized graphene sheets embedded in chitosan nanocomposite membranes for ethanol and isopropanol dehydration via pervaporation, *Ind. Eng. Chem. Res.* 53 (2014) 14474–14484.
- [15] D.P. Suhas, A.V. Raghu, H.M. Jeong, T.M. Aminabhavi, Graphene-loaded sodium alginate nanocomposite membranes with enhanced isopropanol dehydration performance via a pervaporation technique, *RSC Adv.* 3 (2013) 17120.
- [16] K. Cao, Z. Jiang, J. Zhao, C. Zhao, C. Gao, F. Pan, B. Wang, X. Cao, J. Yang, Enhanced water permeation through sodium alginate membranes by incorporating graphene oxides, *J. Membr. Sci.* 469 (2014) 272–283.
- [17] D. Zhou, Y. Cui, P.-W. Xiao, M.-Y. Jiang, B.-H. Han, A general and scalable synthesis approach to porous graphene, *Nat. Commun.* 5 (2014).
- [18] H.B. Huang, Z.G. Song, N. Wei, L. Shi, Y.Y. Mao, Y.L. Ying, L.W. Sun, Z.P. Xu, X. S. Peng, Ultrafast viscous water flow through nanostrand-channelled graphene oxide membranes, *Nat. Commun.* 4 (2013) 3979.
- [19] N. Wei, X. Peng, Z. Xu, Understanding water permeation in graphene oxide membranes, *ACS Appl. Mater. Interfaces* 6 (2014) 5877–5883.
- [20] E.N. Wang, R. Karnik, Graphene cleans up water, *Nat. Nanotechnol.* 7 (2012) 552–554.
- [21] Y. Wang, X.C. Wang, M. Antonietti, Polymeric graphitic carbon nitride as a heterogeneous organocatalyst: from photochemistry to multipurpose catalysis to sustainable chemistry, *Angew. Chem.-Int. Ed.* 51 (2012) 68–89.
- [22] Y. Zheng, J. Liu, J. Liang, M. Jaroniec, S.Z. Qiao, Graphitic carbon nitride materials: controllable synthesis and applications in fuel cells and photocatalysis, *Energy Environ. Sci.* 5 (2012) 6717–6731.
- [23] V. Berry, Impermeability of graphene and its applications, *Carbon* 62 (2013) 1–10.
- [24] B. Jurgens, E. Irran, J. Senker, P. Kroll, H. Muller, W. Schnick, Melem (2,5,8-triamino-tri-s-triazine), an important intermediate during condensation of melamine rings to graphitic carbon nitride: synthesis, structure determination by X-ray powder diffractometry, solid-state NMR, and theoretical studies, *J. Am. Chem. Soc.* 125 (2003) 10288–10300.
- [25] J.E. Huheey, E.A. Keiter, R.L. Keiter, *Inorganic chemistry: principles of structure and reactivity*, fourth ed., HarperCollins, New York, 1993.
- [26] H. Wu, Q. Gong, D.H. Olson, J. Li, Commensurate adsorption of hydrocarbons and alcohols in microporous metal organic frameworks, *Chem. Rev.* 112 (2012) 836–868.
- [27] D.E. Jiang, V.R. Cooper, S. Dai, Porous graphene as the ultimate membrane for gas separation, *Nano Lett.* 9 (2009) 4019–4024.
- [28] Z.N. Ma, X.D. Zhao, Q. Tang, Z. Zhou, Computational prediction of experimentally possible g-C₃N₃ monolayer as hydrogen purification membrane, *Int. J. Hydrog. Energy* 39 (2014) 5037–5042.
- [29] B.V. Lotsch, M. Doblinger, J. Sehnert, L. Seyfarth, J. Senker, O. Oeckler, W. Schnick, Unmasking melon by a complementary approach employing electron diffraction, solid-state NMR spectroscopy, and theoretical calculations-structural characterization of a carbon nitride polymer, *Chem.-Eur. J.* 13 (2007) 4969–4980.
- [30] S.D. Bhat, T.M. Aminabhavi, Pervaporation separation using sodium alginate and its modified membranes – a review, *Sep. Purif. Technol.* 36 (2007) 203–229.
- [31] P. Niu, L. Zhang, G. Liu, H.-M. Cheng, Graphene-like carbon nitride nanosheets for improved photocatalytic activities, *Adv. Funct. Mater.* 22 (2012) 4763–4770.
- [32] X. Zhang, X. Xie, H. Wang, J. Zhang, B. Pan, Y. Xie, Enhanced photoresponsive ultrathin graphitic-phase C₃N₄ nanosheets for bioimaging, *J. Am. Chem. Soc.* 135 (2012) 18–21.
- [33] X.C. Ma, C.L. Hu, R.L. Guo, X. Fang, H. Wu, Z.Y. Jiang, HZSM5-filled cellulose acetate membranes for pervaporation separation of methanol/MTBE mixtures, *Sep. Purif. Technol.* 59 (2008) 34–42.
- [34] R.W. Baker, J.G. Wijmans, Y. Huang, Permeability, permeance and selectivity: a preferred way of reporting pervaporation performance data, *J. Membr. Sci.* 348 (2010) 346–352.
- [35] X. Wang, K. Maeda, A. Thomas, K. Takanabe, G. Xin, J.M. Carlsson, K. Domen, M. Antonietti, A metal-free polymeric photocatalyst for hydrogen production from water under visible light, *Nat. Mater.* 8 (2009) 76–80.
- [36] S.-W. Bian, Z. Ma, W.-G. Song, Preparation and characterization of carbon nitride nanotubes and their applications as catalyst supporter, *J. Phys. Chem. C* 113 (2009) 8668–8672.
- [37] D.Q. Gao, Q. Xu, J. Zhang, Z.L. Yang, M.S. Si, Z.J. Yan, D.S. Xue, Defect-related ferromagnetism in ultrathin metal-free g-C₃N₄ nanosheets, *Nanoscale* 6 (2014) 2577–2581.
- [38] F. Dong, L.W. Wu, Y.J. Sun, M. Fu, Z.B. Wu, S.C. Lee, Efficient synthesis of polymeric g-C₃N₄ layered materials as novel efficient visible light driven photocatalysts, *J. Mater. Chem.* 21 (2011) 15171–15174.
- [39] Y. Li, G. He, S. Wang, S. Yu, F. Pan, H. Wu, Z. Jiang, Recent advances in the fabrication of advanced composite membranes, *J. Mater. Chem. A* 1 (2013) 10058.
- [40] X. Zhao, Q. Zhang, D. Chen, P. Lu, Enhanced mechanical properties of graphene-based poly (vinyl alcohol) composites, *Macromolecules* 43 (2010) 2357–2363.

- [41] J. Li, L. Shao, L. Yuan, Y. Wang, A novel strategy for making poly(vinyl alcohol)/reduced graphite oxide nanocomposites by solvothermal reduction, *Mater. Des.* 54 (2014) 520–525.
- [42] Y. Shi, S. Jiang, K. Zhou, C. Bao, B. Yu, X. Qian, B. Wang, N. Hong, P. Wen, Z. Gui, Y. Hu, R.K.K. Yuen, Influence of g-C₃N₄ nanosheets on thermal stability and mechanical properties of biopolymer electrolyte nanocomposite films: a novel investigation, *ACS Appl. Mater. Interfaces* 6 (2014) 429–437.
- [43] X.M. Yang, Y.F. Tu, L.A. Li, S.M. Shang, X.M. Tao, Well-dispersed chitosan/graphene oxide nanocomposites, *ACS Appl. Mater. Interfaces* 2 (2010) 1707–1713.
- [44] L. Zhang, Z.P. Wang, C. Xu, Y. Li, J.P. Gao, W. Wang, Y. Liu, High strength graphene oxide/polyvinyl alcohol composite hydrogels, *J. Mater. Chem.* 21 (2011) 10399–10406.
- [45] C.H. Lau, P. Li, F. Li, T.-S. Chung, D.R. Paul, Reverse-selective polymeric membranes for gas separations, *Prog. Polym. Sci.* 38 (2013) 740–766.
- [46] S.N. Liu, G.P. Liu, X.H. Zhao, W.Q. Jin, Hydrophobic-ZIF-71 filled PEBA mixed matrix membranes for recovery of biobutanol via pervaporation, *J. Membr. Sci.* 446 (2013) 181–188.
- [47] W.G. Kim, S. Nair, Membranes from nanoporous 1D and 2D materials: a review of opportunities, developments, and challenges, *Chem. Eng. Sci.* 104 (2013) 908–924.
- [48] Y. Liu, K. Ai, L. Lu, Polydopamine and its derivative materials: Synthesis and promising applications in energy, environmental, and biomedical fields, *Chem. Rev.* 114 (2014) 5057–5115.
- [49] C. Cheng, S. Li, W.F. Zhao, Q. Wei, S.Q. Nie, S.D. Sun, C.S. Zhao, The hydrodynamic permeability and surface property of polyethersulfone ultrafiltration membranes with mussel-inspired polydopamine coatings, *J. Membr. Sci.* 417 (2012) 228–236.
- [50] B.D. McCloskey, H.B. Park, H. Ju, B.W. Rowe, D.J. Miller, B.J. Chun, K. Kin, B. D. Freeman, Influence of polydopamine deposition conditions on pure water flux and foulant adhesion resistance of reverse osmosis, ultrafiltration, and microfiltration membranes, *Polymer* 51 (2010) 3472–3485.
- [51] S.B. Teli, G.S. Gokavi, M. Sairam, T.M. Aminabhavi, Highly water selective silicotungstic acid (H₄SiW₁₂O₄₀) incorporated novel sodium alginate hybrid composite membranes for pervaporation dehydration of acetic acid, *Sep. Purif. Technol.* 54 (2007) 178–186.
- [52] R.S. Veerapur, K.B. Gudasi, M. Sairam, R.V. Shenoy, M. Netaji, K.V.S.N. Raju, B. Sreedhar, T.M. Aminabhavi, Novel sodium alginate composite membranes prepared by incorporating cobalt(III) complex particles used in pervaporation separation of water–acetic acid mixtures at different temperatures, *J. Mater. Sci.* 42 (2007) 4406–4417.
- [53] A. Svang-Ariyaskul, R.Y.M. Huang, P.L. Douglas, R. Pal, X. Feng, P. Chen, L. Liu, Blended chitosan and polyvinyl alcohol membranes for the pervaporation dehydration of isopropanol, *J. Membr. Sci.* 280 (2006) 815–823.
- [54] S.Y. Hu, Y. Zhang, D. Lawless, X. Feng, Composite membranes comprising of polyvinylamine-poly(vinyl alcohol) incorporated with carbon nanotubes for dehydration of ethylene glycol by pervaporation, *J. Membr. Sci.* 417 (2012) 34–44.
- [55] R.Y.M. Huang, C.K. Yeom, Pervaporation separation of aqueous mixtures using crosslinked poly(vinyl alcohol)(pva). II. Permeation of ethanol–water mixtures, *J. Membr. Sci.* 51 (1990) 273–292.
- [56] A. Raisi, A. Aroujalian, T. Kaghazchi, A predictive mass transfer model for aroma compounds recovery by pervaporation, *J. Food Eng.* 95 (2009) 305–312.
- [57] H.M. Guan, T.S. Chung, Z. Huang, M.L. Chng, S. Kulprathipanja, Poly(vinyl alcohol) multilayer mixed matrix membranes for the dehydration of ethanol–water mixture, *J. Membr. Sci.* 268 (2006) 113–122.
- [58] J. Zhao, F. Pan, P. Li, C. Zhao, Z. Jiang, P. Zhang, X. Cao, Fabrication of ultrathin membrane via layer-by-layer self-assembly driven by hydrophobic interaction towards high separation performance, *ACS Appl. Mater. Interfaces* 5 (2013) 13275–13283.
- [59] C. Gao, M. Zhang, J. Ding, F. Pan, Z. Jiang, Y. Li, J. Zhao, Pervaporation dehydration of ethanol by hyaluronic acid/sodium alginate two-active-layer composite membranes, *Carbohydr. Polym.* 99 (2014) 158–165.
- [60] V.T. Magalad, A.R. Supale, S.P. Maradur, G.S. Gokavi, T.M. Aminabhavi, Preyssler type heteropolyacid-incorporated highly water-selective sodium alginate-based inorganic–organic hybrid membranes for pervaporation dehydration of ethanol, *Chem. Eng. J.* 159 (2010) 75–83.
- [61] M.B. Patil, R.S. Veerapur, S.A. Patil, C.D. Madhusoodana, T.M. Aminabhavi, Preparation and characterization of filled matrix membranes of sodium alginate incorporated with aluminum-containing mesoporous silica for pervaporation dehydration of alcohols, *Sep. Purif. Technol.* 54 (2007) 34–43.
- [62] C. Zhao, Z. Jiang, J. Zhao, K. Cao, Q. Zhang, F. Pan, High pervaporation dehydration performance of the composite membrane with an ultrathin alginate/poly(acrylic acid)–Fe₃O₄ active layer, *Ind. Eng. Chem. Res.* 53 (2014) 1606–1616.
- [63] S.G. Adoor, L.S. Manjeshwar, S.D. Bhat, T.M. Aminabhavi, Aluminum-rich zeolite beta incorporated sodium alginate mixed matrix membranes for pervaporation dehydration and esterification of ethanol and acetic acid, *J. Membr. Sci.* 318 (2008) 233–246.
- [64] S.D. Bhat, N.N. Mallikarjuna, T.M. Aminabhavi, Microporous aluminophosphate (AlPO₄-5) molecular sieve-loaded novel sodium alginate composite membranes for pervaporation dehydration of aqueous-organic mixtures near their azeotropic compositions, *J. Membr. Sci.* 282 (2006) 473–483.
- [65] C.K. Yeom, K.H. Lee, Characterization of sodium alginate and poly(vinyl alcohol) blend membranes in pervaporation separation, *J. Appl. Polym. Sci.* 67 (1998) 949–959.
- [66] C.K. Yeom, J.G. Jegal, K.H. Lee, Characterization of relaxation phenomena and permeation behaviors in sodium alginate membrane during pervaporation separation of ethanol–water mixture, *J. Appl. Polym. Sci.* 62 (1996) 1561–1576.
- [67] C.K. Yeom, K.H. Lee, Characterization of permeation behaviors of ethanol–water mixtures through sodium alginate membrane with crosslinking gradient during pervaporation separation, *J. Appl. Polym. Sci.* 69 (1998) 1607–1619.